ACADEMIA ROMÂNĂ
*Revue Roumaine de Chimie*
http://web.icf.ro/rrch/

*Rev. Roum. Chim.*,
**2021**, *66*(5), 463–473
DOI: 10.33224/rrch.2021.66.5.10

# MgO OBTAINED BY CHEMICAL AND GREEN SYNTHESIS METHODS AND APPLIED IN PHOTOCATALYTIC DEGRADATION OF METHYL ORANGE

Dana GINGAŞU,* Ioana MÎNDRU, Daniela C. CULIŢĂ, Luminiţa PREDOANĂ, Gabriela PETCU, Mădălina CIOBANU, Silviu PREDA, Jeanina PANDELE-CUŞU and Simona PETRESCU

"Ilie Murgulescu" Institute of Physical Chemistry, Roumanian Academy, 202 Splaiul Independentei, 060021 Bucharest, Roumania

*Received March 19, 2021*

In the present study, the effect of two different approaches: chemical and green synthesis on the properties of MgO nanoparticles was investigated. The green approach was based on the solution combustion method, using aqueous and alcoholic extracts of cinnamon bark, while the chemical one used the precursor method *via* tartarate and gluconate routes. Two types of complex precursors of MgO: $(NH_4)[Mg(C_4O_6H_4)(C_4O_6H_5)]\cdot 7H_2O$ and $[Mg(C_6O_7H_{11})_2]\cdot NH_4NO_3\cdot 5H_2O$ have been isolated and investigated by elemental chemical analysis, IR spectroscopy and thermal analysis. The structure, morphology and textural properties of MgO powders obtained by the two methods were investigated by X-ray diffraction (XRD), infrared spectroscopy (IR), ultraviolet–visible spectroscopy (UV-Vis), scanning electron microscopy (SEM) and nitrogen adsorption – desorption analysis. XRD indicated the obtaining of cubic MgO as single phase with average crystallite sizes between 5.9 and 15.4 nm regardless of the method used. The MgO powders were tested in photocatalytic degradation of methyl orange (MO) dye under ultraviolet and visible light irradiation. The highest degradation efficiency of MO (95%) was noticed under UV irradiation for MgO sample prepared by solution combustion method using alcoholic cinnamon extract.

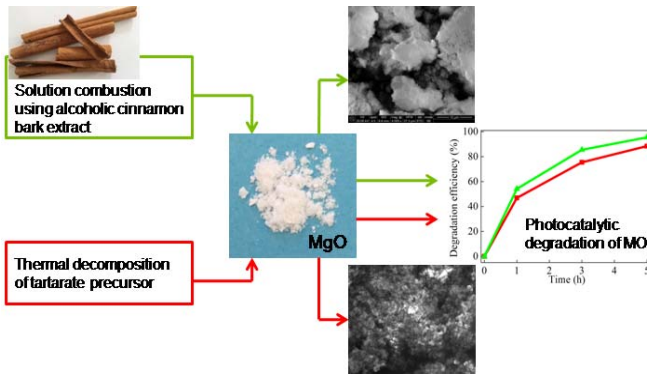


## INTRODUCTION

Among the metal oxides, magnesium oxide (MgO) has attracted attention of researchers due to its remarkable properties: crystal morphology, high surface reactivity, chemical and thermal stability, stable permittivity under low temperatures, optical properties, antibacterial and anticancer activity.[1,2] These properties give to MgO the possibility to be used in various application domains.[3-5] In the field of photocatalysis, MgO is used for the photodegradation of methyl orange (MO),[6,7] methylene blue (MB), Congo red,[8-10] Malathion and orange G.[11]

Over time, many synthesis methods were developed to obtain MgO nanoparticles, such as: solid state reaction,[10] sol-gel,[12] combustion process,[13] hydrothermal,[9] coprecipitation/precipitation[4,11] and microwave-assisted method.[9] Among the soft chemical methods used to synthesize the magnesium oxide nanoparticles, the precursor (thermal decomposition of coordination compounds) and the solution combustion method are the most promising ones. These methods are used due to its advantages: high purity and very good homogeneity of the obtained oxide materials, small particle size and narrow particle size distribution, simplicity of the processes, low costs.[14]

* Corresponding author: d_gingasu@yahoo.com

In the context in which the level of environmental pollution increases from year to year, the development of simpler and cleaner approaches for the synthesis of nano oxides is required. A bridge between soft chemical procedures and eco-friendly approaches can be brought by of nontoxic, environmentally friendly and renewable fuels such as plant extracts and their components, plant-derived materials. The literature from recent years showed that a variety of plant extracts can be used to obtain MgO nanoparticles.[2,3,8,15,16]

The literature data mentioned that metal and metal oxide (Ag, $TiO_2$,) nanoparticles have been synthesized by eco-friendly green methods using cinnamon (*Cinnamon zeylanicum*) bark extract.[17,18] Recently, cinnamon bark extract was used to synthesize cobalt aluminate nanoparticles.[19] The chemical constituents of cinnamon bark extract including terpenoids, like eugenol, linalool, and methyl chavicol, resinous compounds, cinnamic acid, cinnamaldehyde, cinnamyl acetate, ethyl cinnamate and caryophyllene and some protein, work as capping/reducing agents during synthesis. It is assumed that the terpenoids, especially eugenol, which was detected as one of the major components in the extract, play an important role in nanoparticles biosynthesis.[20] Paliwal et al. investigated the presence of chemical constituents in various types extracts (chloroform, butanol, methanol, ethanol, aqueous) of *Cinnamomum zeylanicum* bark.[21]

Based on these considerations, the current study is focused on the synthesis of MgO nanoparticles by the precusor method *via* tartarate and gluconate routes, and by a green approach of solution combustion method using cinnamon bark extract as fuel. The photocatalytic efficiency of MgO obtained by these methods is also comparatively evaluated in methyl orange degradation.

## EXPERIMENTAL

### 1. Reagents

The chemicals: $Mg(NO_3)_2{\cdot}6H_2O$, tartaric acid ($C_4O_6H_6$) and δ-gluconolactone ($C_6H_{10}O_6$) (Merck – Germany), methanol (Lach-ner – Czech Republic), and absolute ethanol (Chimreactiv, Romania) were of reagent quality. Cinnamon barks were collected from local market.

### 2. Synthesis of MgO

#### *MgO nanoparticles obtained by precursor method*

To obtain MgO by the precursor method, two ways were chosen: tartarate and gluconate route, following a protocol described previously.[22] In this case, the following systems were investigated: $Mg(NO_3)_2{\cdot}6H_2O$: $C_4O_6H_6$ and $Mg(NO_3)_2{\cdot}6H_2O$: $2C_6O_7H_{12}$.

The tartarate precursor was synthesized as follows: 1.28 g of $Mg(NO_3)_2{\cdot}6H_2O$ was dissolved in 10 mL of distilled water. This solution was mixed with a tartaric acid solution obtained from 0.75 g tartaric acid and 10 mL distilled water. The amounts used correspond to 1:1 ($Mg^{2+}$: $C_4O_6H_4^{2-}$) molar ratio. After adding methanol and raising the pH to 7 with a mixture of $NH_4OH$:$CH_3OH$ (1:1), a white precipitate formed in solution. The suspension was kept at 4 °C for 24 hours, then filtered and dried over $P_4O_{10}$.

To obtain gluconate precursor, an aqueous solution of gluconic acid ($C_6O_7H_{12}$) obtained by the hydrolysis of 3.56 g δ-gluconolactone ($C_6H_{10}O_6$) at 80 °C, was mixed with an aqueous solution of $Mg(NO_3)_2{\cdot}6H_2O$ (2.56 g $Mg(NO_3)_2{\cdot}6H_2O$ dissolved in 20 mL distilled water) in 1:2 ($Mg^{2+}$:$C_6O_7H_{11}^-$) molar ratio. $NH_4OH$:$CH_3OH$ (1:1) was added to this solution until the pH raised to 6. A white compound precipitated after adding acetone. After 24 hours at 4 °C, the precipitate was separated and dried in air.

Elemental chemical analysis of the precursors:
Tartarate precursor (**1**): Found: C%: 20.83; N%: 3.03; H%: 5.73; Calculated: C%: 20.65; N%: 3.01; H%: 5.80.
Gluconate precursor (**2**): Found: C%: 28.22; N%: 5.34; H%: 7.03; Calculated: C%: 28.57; N%: 5.55; H%: 7.14.

#### *MgO nanoparticles obtained by solution combustion using aqueous and alcoholic cinnamon bark extracts*

To obtain magnesium oxide by green chemistry approach two types of cinnamon bark extract were used, aqueous and alcoholic. The aqueous extract of cinnamon bark (**E1**) was obtained in the same manner presented previously:[19] a mixture of 2.5 g cinnamon powder (2.5 g) and 100 mL distilled was boiled for 5 min. After filtration, the obtained extract (pH = 6) was cooled at room temperature.

The alcoholic extract (**E2**) was obtained by refluxing cinnamon bark powder (2.5 g) in 100 mL ethanol for 15 minutes. After vacuum filtration, the orange alcoholic extract was obtained.

1.28 g of $Mg(NO_3)_2{\cdot}6H_2O$ was dissolved in the cinnamon aqueous extract (**E1**) under stirring for 4 h. This solution was evaporated in oven at 80 °C then the obtained dry residue was thermally treated in furnace at 700 °C/1h. A voluminous white powder of MgO was formed (**ME1** sample). The same amount of $Mg(NO_3)_2{\cdot}6H_2O$ was dissolved in 100 mL alcoholic cinnamon extract (**E2**), under reflux for 2 hours. The solution was evaporated to dryness in a rotary evaporator then the brown red compound was calcined at 700 °C/1h to obtain MgO (**ME2** sample).

### 3. Characterization techniques

The C, N and H content were obtained using a Carlo Erba Model 1108 CHNS-O elemental analyzer. The infrared (IR) spectra of the precursors and MgO powders were recorded on KBr pellets using a JASCO FTIR 4700 spectrophotometer in the 4000 – 400 $cm^{-1}$ range. The thermal behavior of the coordination compounds was analyzed by TG/DTG/DTA methods. Thermo-differential analyses (TG/DTA) were recorded with Mettler Toledo TGA/SDTA $851^e$ apparatus in air atmosphere, with an 80 mL $min^{-1}$ flow rate, using an alumina crucible. The temperature range was set between 25 and 900 °C at a heating rate of 10 °C·$min^{-1}$. The X-ray diffraction (XRD) patterns of the oxide powders were recorded using Rigaku's Ultima IV multipurpose diffraction

system. The diffractometer was set in a parallel beam geometry, using Cu Kα radiation (λ = 1.5406 Å), CBO optics and operated at 40 kV and 30 mA, 0.02º step size and 2º $min^{-1}$ scan speed. The lattice constants were refined using Whole Powder Pattern Fitting (WPPF) and the crystallite size was calculated by the Williamson-Hall method. Samples morphology was assessed using a scanning electron microscope (SEM), Quanta 3D FEG model, operating in high-vacuum mode. Secondary electron images were recorded at accelerating voltage of 20 kV, on the samples placed on stubs and scanned without coating. Nitrogen adsorption-desorption isotherms were recorded at -196 °C using a Micromeritics ASAP 2020 analyzer, on the samples previously degassed at 250 °C for 4 hours under vacuum. The ultraviolet-visible (UV-Vis) spectra in the range 200–800 nm were recorded on a JASCO V570 spectrophotometer, using spectralon as reference. The measurements were carried out in the range 800–200 nm. The result of the optical absorption energies measurements for MgO samples were obtained using the Kubelka-Munk function by plotting $[F(R)hv]^2$ *versus* photon energy (eV).

#### 4. Photocatalytic performance

The photocatalytic degradation of methyl orange (MO) dye in aqueous solution was performed in a quartz microreactor using photocatalysts under visible (380–750 nm) or UV radiation (filter for λ=254 nm) for 1, 3 and 5 h, respectively. 10 mL MO dye solution ($1\times10^{-5}$ M, pH = 5) and 5 mg photocatalyst were added in a quartz reactor. Before irradiation, the suspensions were magnetically stirred in dark for 30 min to ensure the adsorption of MO dye over the photocatalyst surface. Then, the reactor was exposed to irradiation under stirring and ambient conditions. At specific time intervals, aliquots from the suspension was taken out and filtrate in order to separate the catalyst. The degradation process was evaluated by the strength of the maximum absorbance of MO at 464 nm (JASCO V-570 UV-VIS spectrometer). The degradation rate was calculate using the relation $(A_0–A)/A_0*100$, where $A_0$ is the absorbance recorded after dark experiment and A the absorbance value after the photodegradation at a specific time.[23] The adsorption experiments were performed similarly, but without any light irradiation source. The adsorption capacity (Qt) of MgO samples was calculated using the relation: $Qt=(C_0–C_t)\cdot V/m$,[24] where $C_0$ is the concentration of initial MO solution ($10^{-5}$ M), $C_t$ is the concentration of MO solution after 1h of adsorption, V is the volume of solution (10 mL) and m is the mass of MgO materials (0.005 g).

## RESULTS AND DISCUSSION

MgO nanoparticles were obtained by the precursor method through tartarate and gluconate routes and by the solution combustion method using aqueous and alcoholic extracts of cinnamon bark (Scheme 1).

### 1. Characterization of tartrate / gluconate precursors

To establish the molecular formulas of the tartarate/gluconate precursors, the results of elemental chemical analysis were correlated with the IR spectra and thermal analysis.

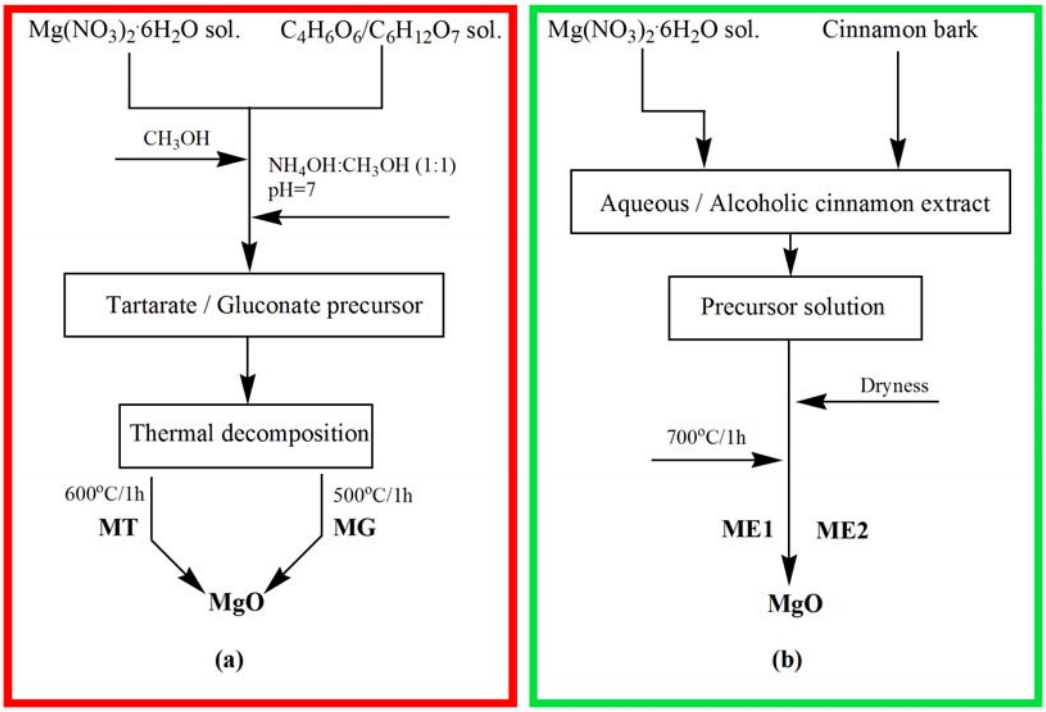


Scheme 1 – A general representation of (a) precursor method,
(b) solution combustion method using aqueous and alcoholic extracts of cinnamon bark, to obtain MgO.

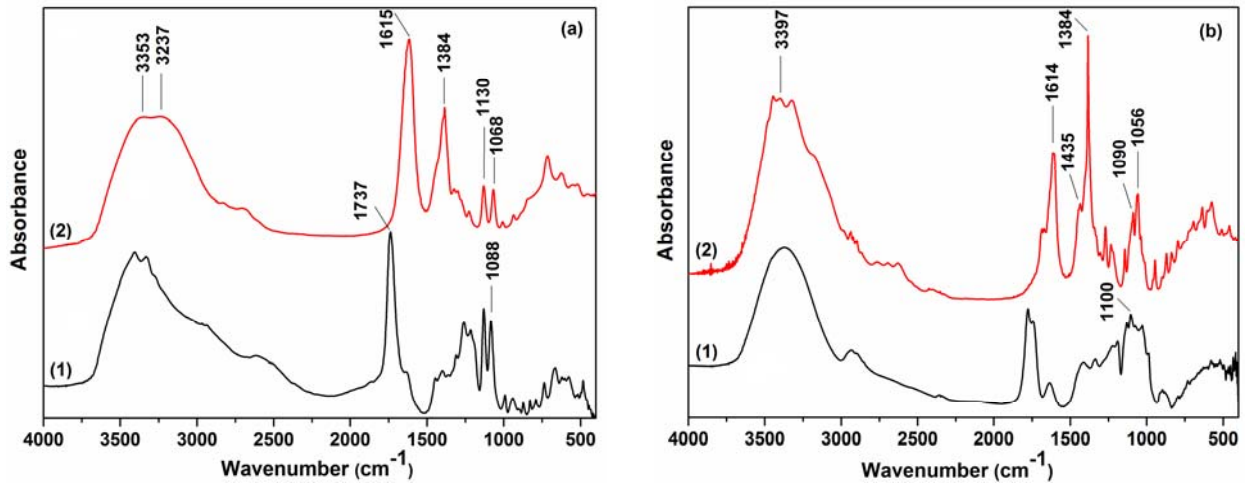


Fig. 1 – IR spectra of: a) tartaric acid (curve 1) and tartarate precursor **1** (curve 2), b) gluconic acid (curve 1) and gluconate precursor **2** (curve 2).

The IR spectra of the precursors along with those of tartaric and gluconic acids are presented in Fig. 1.

Comparing the IR spectrum of the free tartaric acid with that of the tartarate precursor, one can notice that the band at ~ 1737 $cm^{-1}$, attributed to C=O bond of carboxyl group,[25] is replaced in the spectrum of tartarate complex by two bands at 1615 $cm^{-1}$ and 1384 $cm^{-1}$ assigned to carboxylate stretching bands $\nu_{asym}COO^-$ and $\nu_{sym}COO^-$, respectively (Fig. 1a). Applying the spectroscopic criterion,[25] it can be assigned the coordination mode of the carboxylate groups by comparing the magnitude of separation between the asymmetric and symmetric frequencies ($\Delta\nu$) with that corresponding to the sodium salt. In the tartarate precursor $\Delta\nu$ = 231 $cm^{-1}$ is close to $\Delta\nu$ of sodium tartarate (240 $cm^{-1}$) (spectrum not shown here), which allows us to assume a bridging coordination mode of carboxylate groups to the magnesium ion.[26] The band located at ~ 1088 $cm^{-1}$ in the IR spectrum of tartaric acid, characteristic to the stretching vibration of secondary OH groups ($\nu$C-OH) splits in two bands in the spectrum of the precursor (1130 $cm^{-1}$ and 1068 $cm^{-1}$), sustaining the coordination of tartarate anion to the metal ion also by the secondary OH groups. In the IR spectrum of the tartarate precursor, the very intense band at 3353 $cm^{-1}$ is due to the vibration frequencies of the OH groups in water and secondary OH groups, while that at 3237 $cm^{-1}$ can be attributed to the stretching frequency of ammonium group, $\nu(NH_4^+)$.

Analysis of the IR spectrum of magnesium gluconate (Fig. 1b) by comparison with that of gluconic acid, suggests a somewhat different behaviour of gluconate and tartarate ligands. The existence of two very intense bands characteristic to vibration frequencies $\nu_{asym}COO^-$ (1614 $cm^{-1}$) and $\nu_{sym}COO^-$ (1435 $cm^{-1}$) indicates the coordination of the carboxyl group at the magnesium ion. The magnitude of separation ($\Delta\nu$) between these bands (179 $cm^{-1}$), smaller than that of sodium gluconate (233 $cm^{-1}$)[27] suggests a bidentate coordination mode of carboxylate groups of gluconate ligand to the magnesium ions. The band at ~ 1100 $cm^{-1}$ in the spectrum of free gluconic acid splits in two bands, 1090 $cm^{-1}$ and 1056 $cm^{-1}$, in gluconate complex which indicates the participation of one or more OH groups in coordination. The very sharp band at 1384 $cm^{-1}$ can be ascribed to the vibration frequency $\nu(NO_3^-)$, while the large one at 3397 $cm^{-1}$ is due to the vibrations of OH groups in water and / or secondary OH groups.

In order to establish the thermal behaviour of the precursors and optimal conditions for obtaining magnesium oxide, they were subjected to a thermogravimetric study (Fig. 2).

The thermal analysis of the tartarate precursor **1** reveals several decomposition steps, in the 40–600 °C range. The loss of six water molecules and one of ammonia occurs in the range 40–160 °C (27% mass loss). This step is accompanied by an endothermic effect with a maximum of 144 °C on the DTA curve. The second step occurs between 160 and 450 °C and corresponds to the elimination of other water molecules and oxidative degradation of the ligand (60% mass loss); the process is accompanied by one exothermic effect with maximum at 415 °C. Between 450 and 600 °C the mass loss is 4%. At temperatures above 600 °C no other weight loss or thermal effects could be observed.

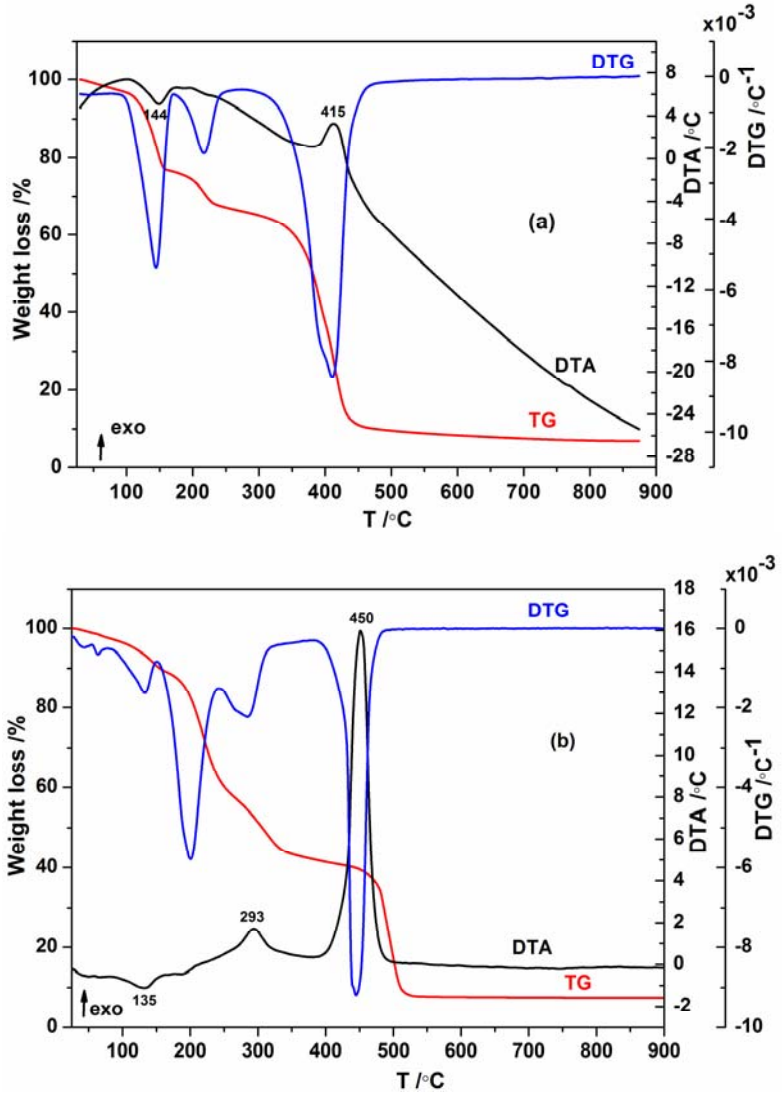


Fig. 2 – TG, DTG and DTA curves of: a) precursor **1**, b) precursor **2**.

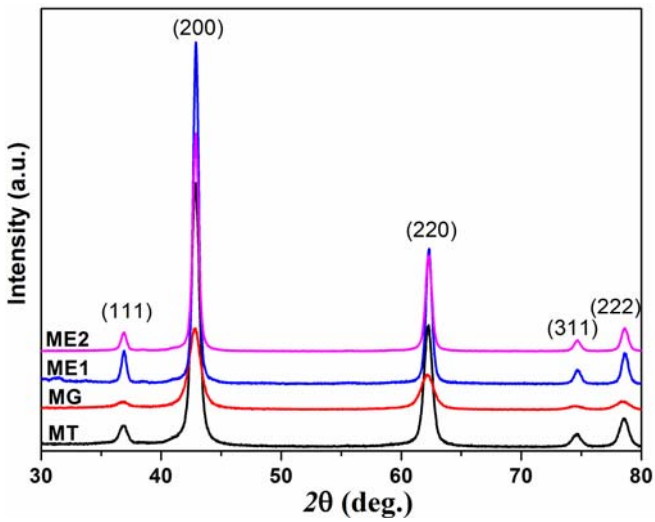


Fig. 3 – X-ray diffraction of MgO powder obtained by precursor method (**MG** and **MT** samples) and solution combustion (green) method (**ME1** and **ME2** samples).

The gluconate precursor **2** decomposes in the range 40–500 °C. The first decomposition step takes place between 40 and 160 °C and an endothermic effect at 135 °C is observed on the DTA curve. At this stage two water molecules are removed (9% mass loss). In the second stage (160–500 °C) two exothermic processes (the first at 293 °C and the second with maximum at 450 °C) are observed on DTA curve. The first exothermal effect corresponds to the elimination of other water molecules and ammonium nitrate decomposition, and the second one corresponds to the degradation / oxidation of the ligand with the formation of MgO. On TG curve for this stage a mass loss of 83% was observed.

Based on these investigations, the following molecular formulas of the complexes have been established: $(NH_4)[Mg(C_4O_6H_4)(C_4O_6H_5)]\cdot 7H_2O$ (tartarate precursor, compound **1**) $[Mg(C_6O_7H_{11})_2]\cdot NH_4NO_3\cdot 5H_2O$ (gluconate precursor, compound **2**).

## 2. Characterization of MgO nanoparticles

In order to obtain MgO (**MT** and **MG** samples), the tartarate precursor was calcined at 600 °C/1h, while the gluconate precursor was calcined at 500 °C/1h.

Fig. 3 shows the XRD patterns of four samples **MT**, **MG**, **ME1** and **ME2** obtained by chemical and green synthesis.

Single phase MgO, with cubic structure (ICDD 00-045-0946, G.S. Fm-3m) was identified in all four samples. The lattice parameter is 4.2212 Å for **MT** sample and 4.2252 Å **MG** sample. The average crystallite size is 10.2 nm for **MT** sample and 5.9 nm for **MG** sample. These values are lower than those obtained for MgO obtained by precipitation using other organic acids[11] (Table 1). Instead, the lattice parameters of MgO obtained by green chemistry approach using aqueous and alcoholic cinnamon extract are 4.2119 Å for **ME1** sample and 4.2127 Å for **ME2** sample. The obtained values are similar with those reported in the literature.[13] The average crystallite sizes are greater than in case of MgO obtained by precursor method (15.4 nm for **ME1** sample and 15 nm for **ME2**), but lower than those reported in literature for MgO obtained using other plant extract.[15]

Fig. 4 shows SEM images of the obtained MgO samples. Due to the very small particle size, a tendency of agglomeration can be observed. As can be seen from SEM images, the crystallites of the **MT** sample are tiny and the shapes of particles are not clearly distinguishable (Fig. 4a). The **MG** sample has a different morphology as illustrated in Fig. 4b. The general appearance consists in stacked flakes with corrugated edges and chunks of solid material. These flakes are intermingled together formed larger flower-shaped conglomerates. Figs. 4c and 4d revealed that MgO samples obtained by green chemistry approach using aqueous and alcoholic cinnamon extract contain aggregates of particles with quasispherical shapes. These particles (smaller in the case of **ME2** sample) seem well crystallized and uniformly distributed.

*Table 1*

Literature survey for the lattice parameter, the crystallite size and the morphology of magnesium oxide obtained by different chemical methods and by green approaches

| **Synthesis method** | **Crystallite size (nm)** | **Lattice parameter (Å)** | **Morphology** | **References** |
|---|---|---|---|---|
| Precipitation method; 650 °C/6 h | 33–60 | – | Weak agglomeration; rectangular shape | 11 |
| Combustion/urea; 1150 °C/2 h | 23–37 | 4.2110–4.2198 | Agglomerates | 13 |
| Hydrothermal method; 400 °C/2 h/ Microwave assisted method; 400 °C/2 h | 14/20 | 4.246/4.247 | Rod/ Spherical shape | 9 |
| Green synthesis method / *Sargassum wighitii* extract / 500 °C/3 h | 43 | – | Agglomerates; flower shape | 8 |
| Green synthesis method / *Solanum trilobatum* extract / 400 °C/8 h | 30 | – | Agglomerates; spherical shape | 15 |
| Tartarate route; 600 °C/1 h | 10.2 | 4.2212 | Agglomerates | This study |
| Gluconate route; 500 °C/1 h | 5.9 | 4.2252 | Flower-shaped conglomerates | This study |
| Green synthesis method / cinnamon extracts / 700 °C/1 h | 15.4/15 | 4.2119/4.2127 | Agglomerates; quasispherical shape | This study |

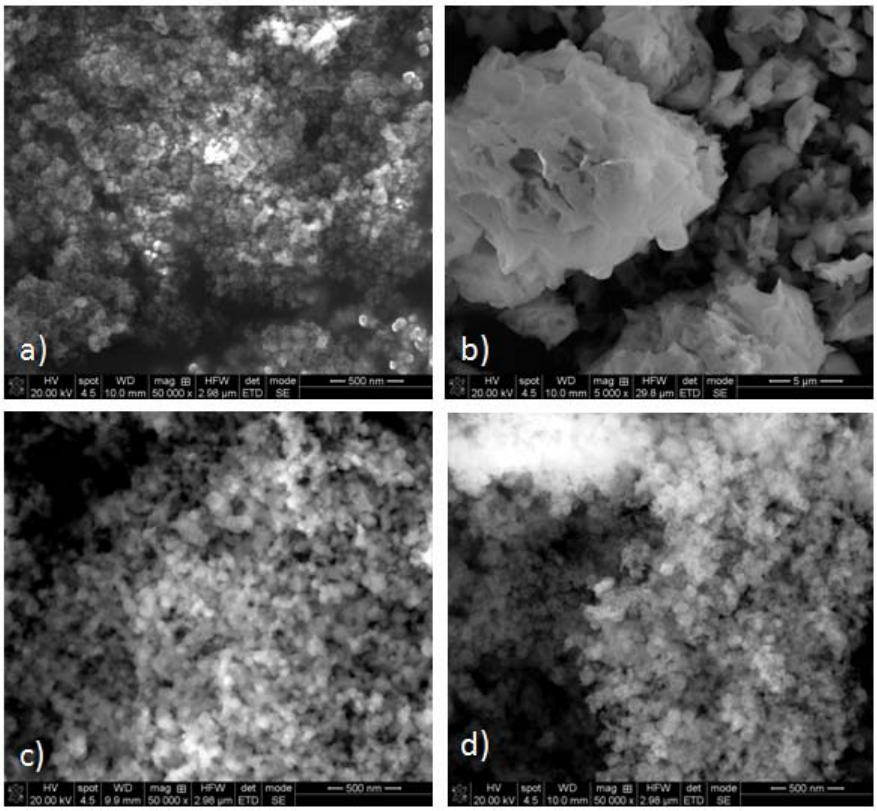


Fig. 4 – SEM images of MgO samples: a) **MT**, (b) **MG**, (c) **ME1**, (d) **ME2**.

The IR spectra of MgO samples show an intense band at ~ 500 nm attributed to the Mg-O vibration frequency, confirming the formation of MgO.

For the textural characterization of MgO samples, the $N_2$ adsorption - desorption isotherms were recorded (Fig. 5). All four isotherms are type IV according to the IUPAC classification,[28] with H3 hysteresis loops, characteristic for mesoporous materials. The values of specific surface area ($S_{BET}$), total pore volume ($V_{total}$) and average pore diameter ($d_{BJH}$) are presented in Table 2. Analyzing the isotherms of **MT** and **MG**, a clear difference is observed between their textural characteristics. In the case of **MG** the isotherm is characterized by the presence of a hysteresis loop starting from 0.4 ($P/P_0$), due to capillary condensation in uniform mesopores of small dimensions. The narrow pore size distribution (inset of Fig. 5b) confirms this observation, the average pore diameter calculated using the desorption branch being 3.5 nm. Pore uniformity leads to a relatively high specific surface area for this type of material (147.7 $m^2g^{-1}$). In the case of **MT** the allure of the isotherm is different, the capillary condensation appearing at relative pressures higher than 0.75. This behaviour is characteristic for materials with relatively large mesopores. The calculated average pore diameter is 22.9 nm. The shape of the hysteresis loop can be associated with the presence of slit shaped pores. Analyzing the thermal behaviour of these two samples, it can be said that the differences between them in terms of porosity can be attributed to the decomposition of the precursor. In the case of **MG** the thermal decomposition of the precursor occurs slowly, in the temperature range r.t. - 520 ºC, while in the case of **MT**, the precursor decomposes faster, in a smaller temperature range (r.t. - 450 ºC), with a more sudden evolution of the gas obtained by decomposition. This behaviour explains the different values of the total pore volume of the samples (Table 2).

The higher $S_{BET}$ value and the narrower pore size distribution in the case of **MG** suggest an ordered structure of the coordination compound precursor of MgO. The gluconate anion can be considered as a directing agent (template agent) of MgO structure. Not the same can be said about the tartarate anion, because MgO obtained by decomposing the corresponding precursor has a wide pore size distribution, with a relatively large average pore diameter (22.9 nm).

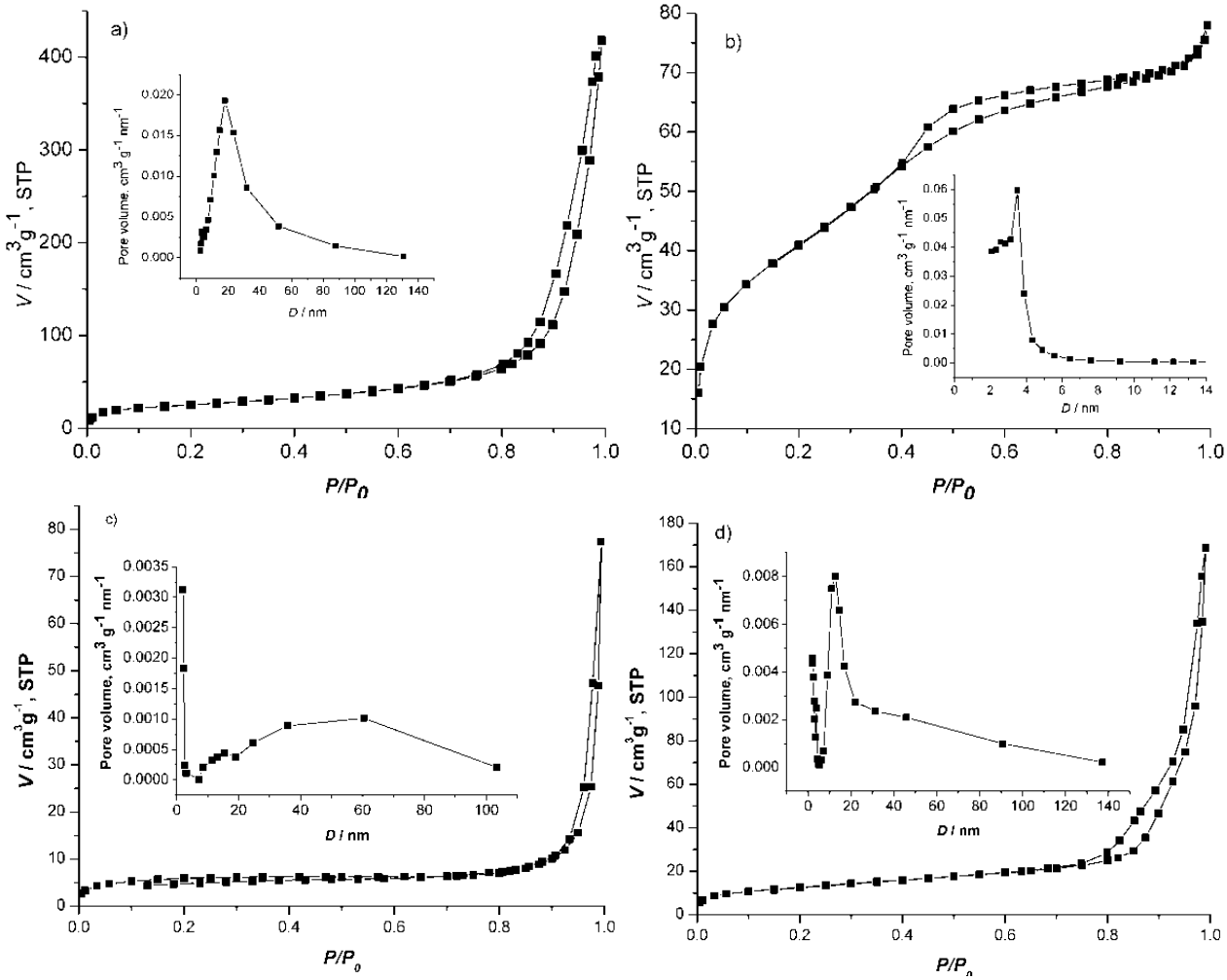


Fig. 5 – $N_2$ adsorption–desorption isotherms and pore size distribution (inset) of MgO samples (a) **MT**; (b) **MG**; (c) **ME1**; (d) **ME2**.

*Table 2*

The textural parameters, optical absorption energies (E) and MO adsorption capacity (Qt) of the MgO samples

| Sample | $S_{BET}$ ($m^2g^{-1}$) | $V_{total}$ ($cm^3g^{-1}$) | $d_{BJH}$ (nm) | E (eV) | Qt (mg/g) |
|---|---|---|---|---|---|
| **MT** | 89.1 | 0.646 | 22.9 | 2.27 | 672 |
| **MG** | 147.7 | 0.120 | 3.5 | 2.41 | 840 |
| **ME1** | 21.2 | 0.120 | 40.0 | 1.25 | 64 |
| **ME2** | 45.0 | 0.260 | 22.2 | 1.44 | 516 |

For MgO samples obtained using cinnamon extracts (aqueous and alcoholic), the $S_{BET}$ values are substantially lower than those of MgO obtained from tartrate and gluconate precursors. The aqueous cinnamon extract leads to an almost non-porous MgO, the hysteresis loop having a very small area. By using the alcoholic extract, the specific surface area and the total pore volume of MgO are doubled (see Table 2). A possible explanation could be based on the composition of the extracts. The alcoholic extract contains a larger amount of organic components which, by decomposition, can generate a large amount of gases with a porogen role. The pore size distribution covers and even slightly exceeds the specific mesopore range, the peak maximum being at ~ 12 nm.

The UV-Vis measurements of the samples are shown in Fig. 6. It can be observed the presence of a characteristic absorption band at 270 nm, assigned to MgO nanoparticles[29] *via* both proposed methods. Furthermore, for all the samples it was evidenced a redshift of the absorption edges (Fig. 6) compared to other chemically-synthesized MgO NPs.[30-32]

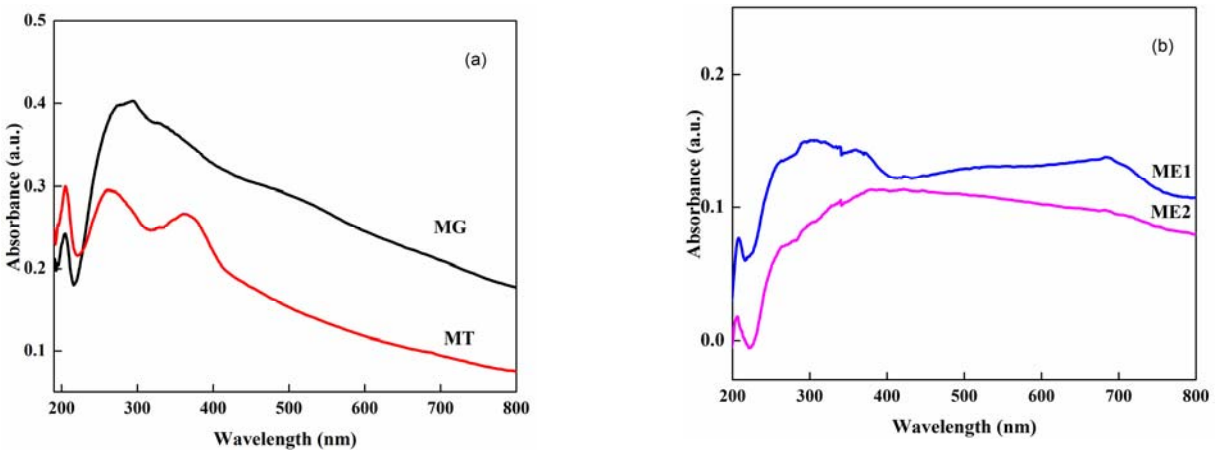


Fig. 6 – UV-Vis spectra of MgO obtained by: a) precursor method, b) solution combustión method.

**MT** and **MG** samples exhibited more intense absorption bands between 200 and 400 nm, compared to **ME1** and **ME2** samples. The UV absorption peaks at 205 and ~260 nm can be ascribed to excitation of $O^{2-}$ surface anions on the edge and on the corner of the nanocrystal, respectively.[33]

The values of the optical absorption energies (E) are presented in Table 2.

## 3. MgO application in methyl orange degradation reaction

In the present work, MO dye was used as model pollutant to evaluate the photocatalytic activity of MgO samples under UV and visible light irradiation. Efficiency of the photocatalytic degradation of MO aqueous solution using synthesized MgO materials under UV and Vis light irradiation is shown in Fig. 7.

It was observed that photocatalytic activity for all the samples was better under UV irradiation than under visible light. Also, Fig. 7 evidenced that **ME2** sample with crystallite size of 15 nm was the most effective in photocatalytic degradation, removing a total of 95% of the dye in 300 min (Fig. 7a), while **ME1** with a similar value of crystallite size (15.4 nm), but with a smaller surface area presented a lower degradation efficiency of about 85%. After 5 hours of irradiation, the lowest degradation efficiency was observed in the case of **MG** sample, even if the photocatalytic results recorded after 1 hour were not much lower than in the case of **ME1** sample. This can be attributed to its relatively low average pore diameter (3.5 nm) which leads to a rapid blockage of the pore entries by adsorption of methyl orange and, consequently, to the blocking of light penetration to active sites. Furthermore, as SEM images revealed in the case of **MG** photocatalyst, the particles are much smaller than the other samples, assembled in thin aggregates (like flakes), united in much larger flower-shaped conglomerates. These morphologies leads to a decrease of the photocatalytic efficiency, because the aggregation impedes the transfer of photo-generated charge carriers to surface and increase the probability of recombination.[34]

The surface charge of MgO, which is influenced by the pH of the solution, is a key factor in the MO adsorption process. When the pH of MO solution is equal to 5, the surface of MgO oxide is positively charged[35,36] and adsorption is the result of electrostatic interactions with anionic MO molecules. As shown in Table 2, the highest adsorption capacity of 840 mg/g was evidenced for **MG** sample after 1 hour. This is due to its highest surface area (147.7 $m^2/g$) which ensures the availability of a large number of active sites for MO molecules.

The photocatalytic performances of the synthesized materials under UV and visible light irradiation were also evaluated through the MO degradation kinetics studies. These results are presented in Fig. 8.

The MO degradation in the presence of synthesized photocatalysts under UV and visible irradiation follows a pseudo first order mechanism (also known as Langmuir-Hinshelwood kinetic model), expressed as $\ln(C_0/C) = k_{app}t$, where $k_{app}$ is the apparent rate constant of the photodegradation process, $C_0$ and C represent MO concentrations (mg/L) at the initial time and a given time t (min), respectively. The kinetics results (Fig. 8) evidenced the highest values of apparent rate constant $k_{app}$ for **ME2** sample (0.0105 $min^{-1}$ for UV irradiation and 0.0048 $min^{-1}$ for Vis irradiation).

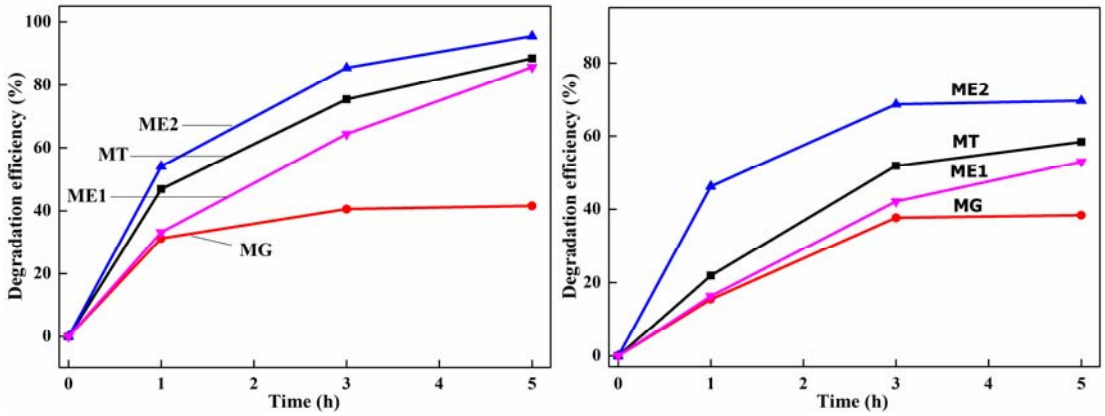


Fig. 7 – Photocatalytic degradation of MO under: a) UV light irradiation, b) Visible light irradiation.

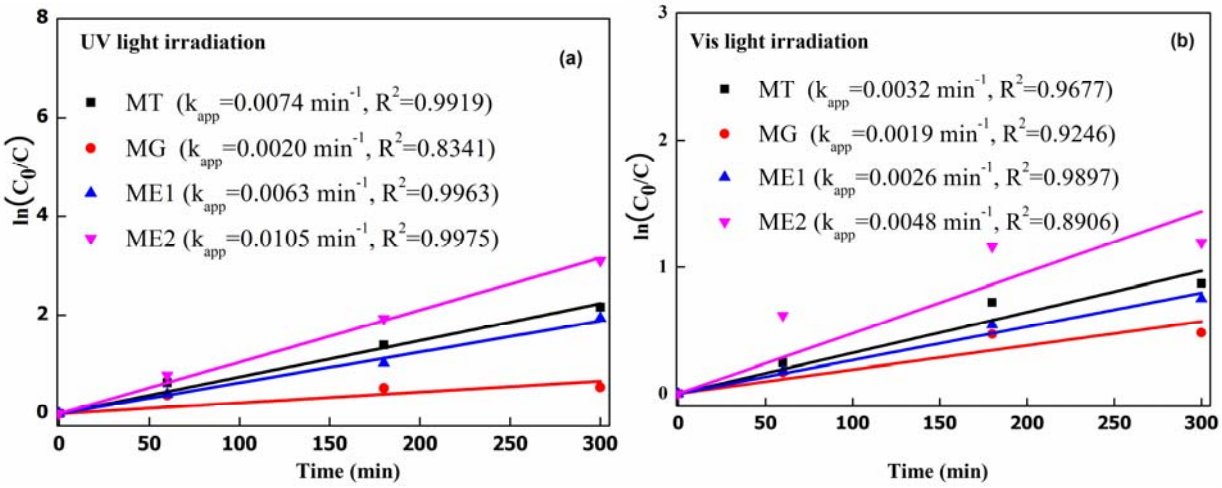


Fig. 8 – Kinetic and apparent rate constant kapp values of MO photocatalytic degradation under: a) UV light irradiation, b) Vis light irradiation.

## CONCLUSIONS

Two different approaches have been used to synthesize MgO nanoparticles: (i) the precursor method via tartarate and gluconate routes and (ii) the solution combustion method using aqueous and alcoholic cinnamon bark extracts as fuels. The precursors of the MgO samples were isolated and characterized. The MgO samples (**MT**, **MG**, **ME1** and **ME2**) were characterized by various techniques. It was shown that both precursor and solution combustion methods lead to the formation of MgO with cubic structure and average crystallite size between 5.9 and 15.4 nm. The specific surface areas of the MgO obtained by the precursor method are significantly higher than those obtained by solution combustion method. The photocatalytic activity of the MgO samples towards the degradation of methyl orange was evaluated. The results illustrate that the MgO nanoparticles synthesized in this study are promising photocatalysts for degradation of methyl orange in aqueous solution. The highest degradation efficiency (95%) was obtained for MgO synthesized by green chemistry approach using alcoholic cinnamon bark extract (**ME2**).

*Acknowledgements:* This work was supported by a grant of the Roumanian Ministry of Research and Innovation, PCCDI-UEFISCDI, project number PN-III-P1-1.2-PCCDI-2017-0476/51PCCDI/2018, within PNCDI III. The work also benefits from the support of the "Materials Science and Advanced Characterization Methods" Programme of the "Ilie Murgulescu" Institute of Physical Chemistry, financed by the Roumanian Academy.

## REFERENCES

1. J. P. Singh, S. H. Kim, H. K. Kang, S. O. Won, I.-J. Lee and K. H. Chae, *Mater. Chem. Front.*, **2018**, *2*, 1707–1715.
2. M. A. Ammulu, K. V. Viswanath, A. K. Giduturi, P. K. Vemuri, U. Mangamuri and S. Poda, *J. Genet. Eng. Biotechnol.*, **2021**, *19*, Art. Number 21.

3. J. Suresh, G. Pradheesh, V. Alexramani, M. Sundrarajan and S. I. Hong, *Adv. Powder Technol*., **2018**, *29*, 1685–1694.
4. M. M. Imani and M. Safaei, *J. Nanotechnol*., **2019**, *2019*, 6063832.
5. R. Vandamar Poonguzhali, E. Ranjith Kumar, T. Pushpagiri, A. Steephen, N. Arunadevi and S. Baskoutas, *Solid State Commun*., **2021**, *325*, 114161.
6. R. Dobrucka, *Iran J. Sci. Technol. Trans. Sci.*, **2018**, *42*, 547–555.
7. K. N. Shravana Kumara, H. P. Nagaswarupa, K. R. Vishnu Mahesh, S. C. Prashantha, M. Mylarappa and D. M. K. Siddeshwara, *Nanosystems: Phys. Chem. Math*., **2016**, *7*, 662–666.
8. A. Pugazhendhi, R. Prabhu, K. Muruganantham, R. Shanmuganathan and S. Natarajan, *J. Photochem. Photobiol. B: Biology*, **2019**, *190*, 86–97.
9. K. Karthik, S. Dhanuskodi, C. Gobinath, S. Prabukumar and S. Sivaramakrishnan, *J. Photochem. Photobiol. B: Biology*, **2019**, *190*, 8–20.
10. M. Chamack, A. R. Mahjoub and A. Hosseinian, *Nanochem. Res*., **2018**, *3*, 85–91.
11. I. M. I. Moustafa, I. A. Saleh and M. R. Abdelhamid, *Material Sci Eng*., **2017**, *6*, 100359.
12. N. Rani, S. Chahal, A. S. Chauhan, P. Kumar, R. Shukla1 and S. K. Singh, *Mater. Today-Proc*., **2019**, *12*, 543–548.
13. I. Ercan, O. Kaygili, T. Ates, B. Gunduz, N. Bulut, S. Koytepe and I. Ozcan, *Ceram. Int.*, **2018**, *44*, 14523–14527.
14. W. Wen and J.-M. Wu, *RSC Adv*., **2014**, *4*, 58090–58100.
15. S. Narendhran, M. Manikandan and P. Baby Shakila, *Bull. Mater. Sci*., **2019**, *42*, 133.
16. E. R. Essien, V. N. Atasie, T. O. Oyebanji and D. O. Nwude, *Chem. Papers*, **2020**, *74,* 2101–2109.
17. G. Nabi, W. Raza and M. B. Tahir, *J. Inorg. Organomet. Polym. Mater*., **2020**, *3,* 1425–1429.
18. S. Anjum, G. Jacob and B. Gupta, *Emergent Mat*., **2019**, *2*, 113–122.
19. D. Gingasu, I. Mindru, L. Patron, G. Marinescu, A. Ianculescu, V.A. Surdu, S. Somacescu, S. Preda and O. Oprea, *Rev. Roum. Chim*., **2018**, *63*, 459–466.
20. A. H. Saliem, O. M. S. Ibrahim and S. I. Salih, *Kufa J. Vet. Med. Sci*., **2016**, *7,* 51–63.
21. R. Paliwal, M. A. Madungurum and N. Dahiru, *Int. J. Eng. Sci. Res. Technol*., **2018**, *7*, 162–170.
22. D. Gingasu, L. Patron, I. Mindru, N. Stanica and I. Balint, *Rev. Roum. Chim.,* **2004**, *49*, 669–674.
23. S. Xie, P. Huang, J. J. Kruzic, X. Zeng and H. Qian, *Sci. Rep*., 2016, *6*, 21947–21956.
24. H. Zhang, J. Hu, J. Xie, S. Wang and Y. Cao, *RSC Adv.*, **2019**, *9*, 2011–2017.
25. K. Nakamoto, "Infrared and Raman Spectra of Inorganic and Coordination Compounds", fourth edition, Wiley, New York, 1986.
26. I. Mindru, D. Gingasu, L. Patron, G. Marinescu, J. M. Calderon-Moreno, L. Diamandescu, M. Secu and O. Oprea, *Mat. Res. Bull*., **2017**, *85*, 240–248.
27. V. D. Nikolić, D. P. Ilić, L. B. Nikolić, L. P. Stanojević, M. D. Cakić, A. D. Tačić and S. S. Ilić-Stojanović, *Advanced technologies*, **2014**, *3,* 16–24.
28. K. S. W. Sing, D. H. Everett, R. A. W. Haul, L. Moscou, R. A. Pierotti, J. Rouquerol and T. Siemieniewska, *Pure Appl. Chem*., **1985**, *57*, 603–619.
29. M. I. Khan, M. N. Akhtar, N. Ashraf, J. Najeeb, H. Munir, T. I. Awan, M. B. Tahir and M. R. Kabli, *Applied Nanosci.*, **2020**, *10*, 2351–2364.
30. L. Aghebati-Maleki, B. Salehi, R. Behfar, H. Saeidmanesh, F. Ahmadian, M. Sarebanhassanabadi and M. Negahdary, *Int. J. Electrochem. Sci*., **2014,** *9*, 257–271.
31. I. V. Matsukevich, I. Atkinson, S. V. Basarab, G. Petcu, S. Petrescu, V. Parvulescu and V. Fruth, *Rom. J. Mater.*, **2019,** *49*, 483 – 490.
32. M. C. C. Wobbe, A. Kerridgeab and M. A. Zwijnenburg, *Phys. Chem. Chem. Phys*., **2014**, *16*, 22052–22061.
33. Z. Liu, Z. Yin, C. Cox, M. Bosman, X. Qian, N. Li, H. Zhao, Y. Du, J. Li and D. G. Nocera, *Sci. Adv.*, **2016**, *2*, e1501425.
34. W. Szeto, C. W. Kan, C. W. M. Yuen, S.-W. Chan and K. H. Lam, *Int. J. Chem. Eng*., **2014**, *2014*, 270946.
35. M. A. Ahmed and Z. M. Abou-Gamra, *Nanotechnol. Environ. Eng.*, **2016**, *1*, 10.
36. S. Ahmed, J. Pan, D. Li, P. Tang, X. Shu and Y. Feng, *Beilstein Arch*., **2020**, 20205.